

Supporting Information for

Direct Air Capture of CO₂ via Cyclic Viologen Electrocatalysis

Shijie Liu,^{‡a} Jinqiang Zhang,^{‡b} Feng Li,^{‡a} Jonathan P. Edwards,^{‡d} Yurou Celine Xiao,^a Dongha Kim,^b Panagiotis Papangelakis,^a Jiheon Kim,^{a,b} David Elder,^a Phil De Luna,^d Mengyang Fan,^a Geonhui Lee,^b Rui Kai Miao,^a **Tanushree Ghosh^a**, **Yu Yan,^b** Yuanjun Chen,^b Yong Zhao,^a **Zunmin Guo,^a** Cong Tian,^b Peihao Li,^b Yi Xu^{*c}, Edward H. Sargent^{*b}, David Sinton^{*a}



Figure S1. Illustration of the Lab-scale air contactor array setup, bubbling air into CVE-regenerated capture solution.



Figure S2. Illustration the formation of a viologen-containing film on the carbon electrode in the H-cell configuration, using 0.02 M BV in 1 M NaCl aqueous electrolyte: The original carbon electrode (left), viologen-containing film becomes visible after electrochemical reduction (dark colour, right).

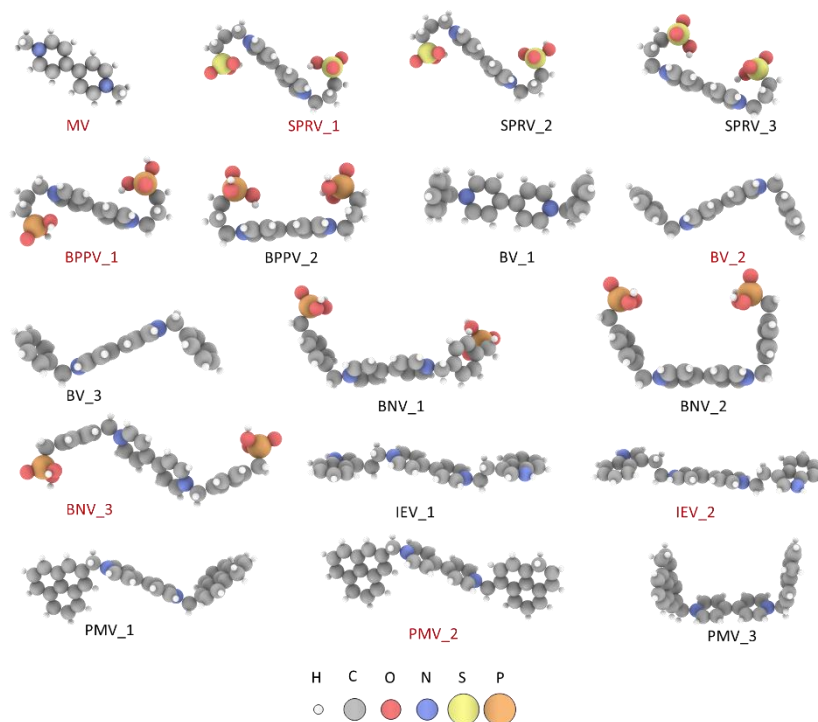


Figure S3. DFT-optimized geometries of various gas-phase viologen molecules under various conformations. The lowest electronic energy state of each molecule is marked in red.

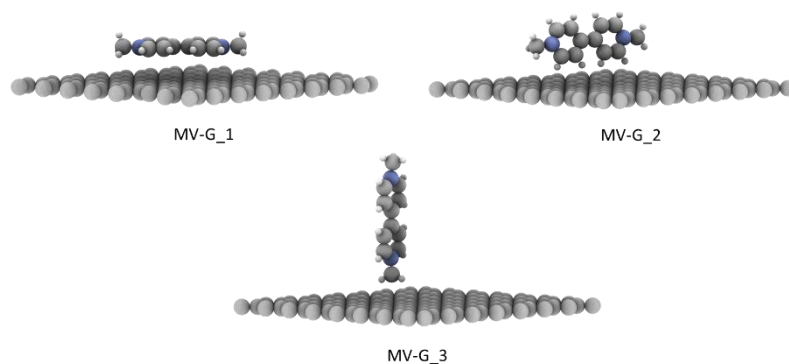


Figure S4. DFT-optimized geometries of carbon electrode with adsorbed MV molecule under various binding configurations.

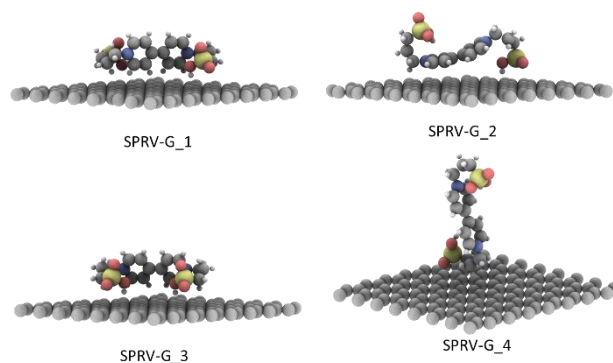


Figure S5. DFT-optimized geometries of carbon electrode with adsorbed SPRV molecule under various binding configurations.

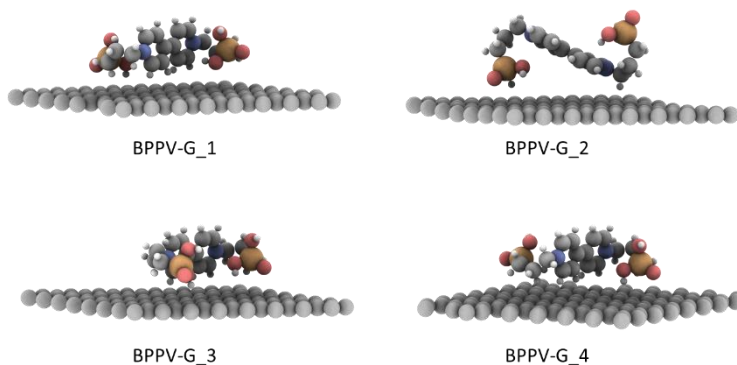


Figure S6. DFT-optimized geometries of carbon electrode with adsorbed BPPV molecule under various binding configurations.

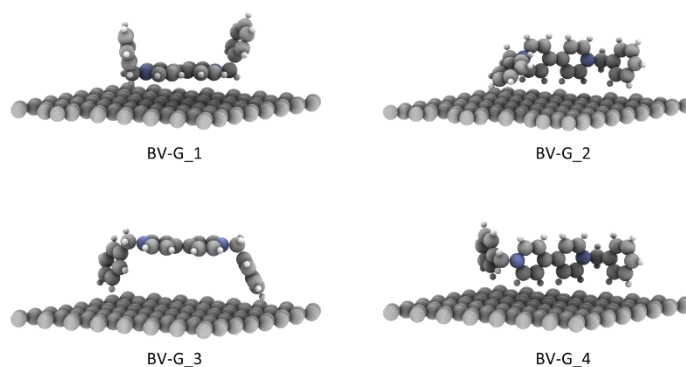


Figure S7. DFT-optimized geometries of carbon electrode with adsorbed BV molecule under various binding configurations.

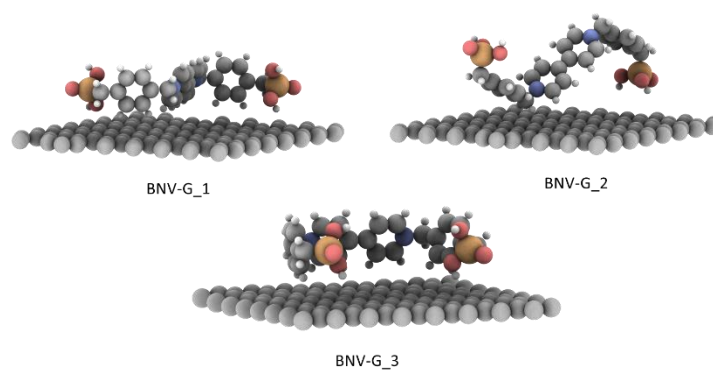


Figure S8. DFT-optimized geometries of carbon electrode with adsorbed BNV molecule under various binding configurations.

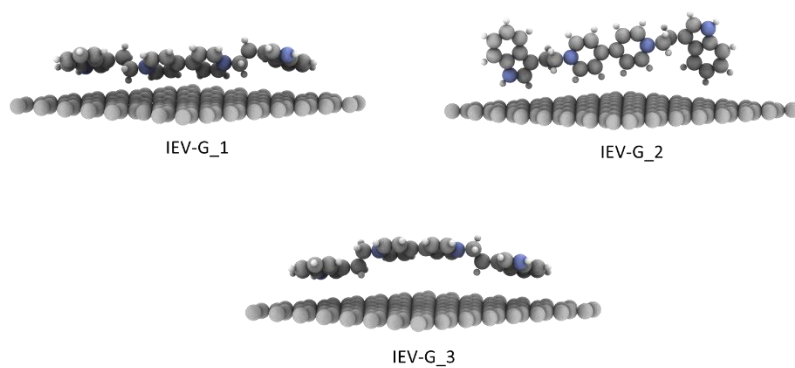


Figure S9. DFT-optimized geometries of carbon electrode with adsorbed IEV molecule under various binding configurations.

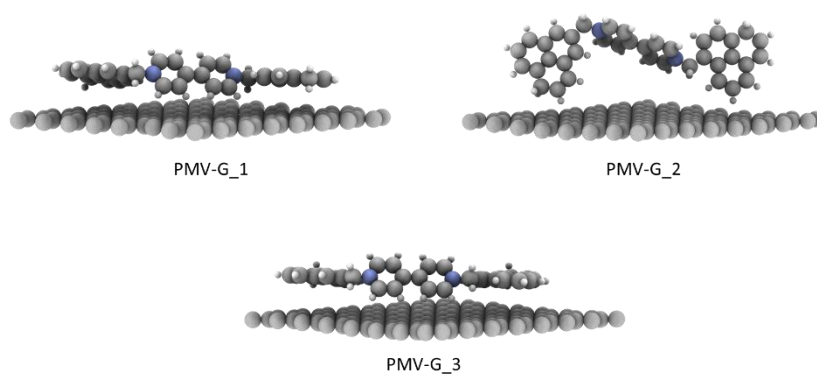


Figure S10. DFT-optimized geometries of carbon electrode with adsorbed PMV molecule under various binding configurations.

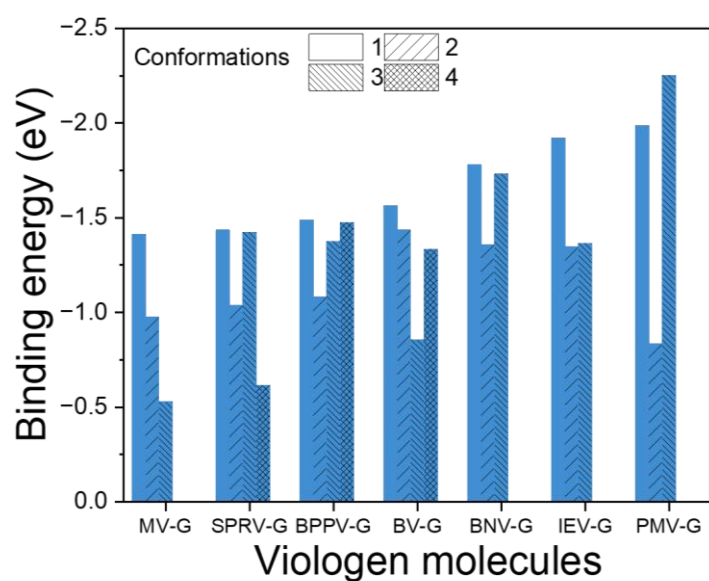


Figure S11. Binding energy of carbon electrode with adsorbed viologen molecule under various binding configurations.

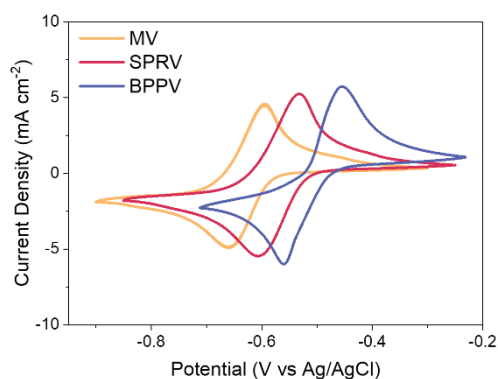


Figure S12. Cyclic voltammetry (CV) studies depict the first electron transfer redox pairs of 0.02 M MV, SPRV, and BPPV in a 1 M NaCl aqueous electrolyte in an H-cell configuration.



Figure S13. Illustration the carbon electrode in the H-cell configuration, using 0.02 M BPPV in 1 M NaCl aqueous electrolyte: The original carbon electrode (left), No viologen-containing film after electrochemical reduction (right).

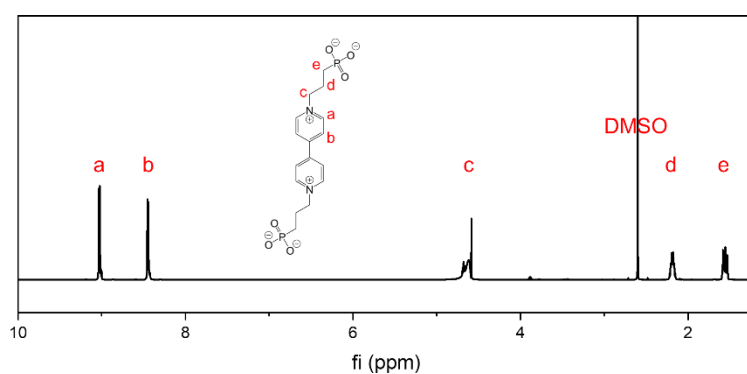


Figure S14. The ^1H NMR spectra of BPPV in DMSO reveals distinct peaks, with the DMSO solvent peak positioned at 2.6 ppm. The labels correlate individual peaks to specific chemical bonds.

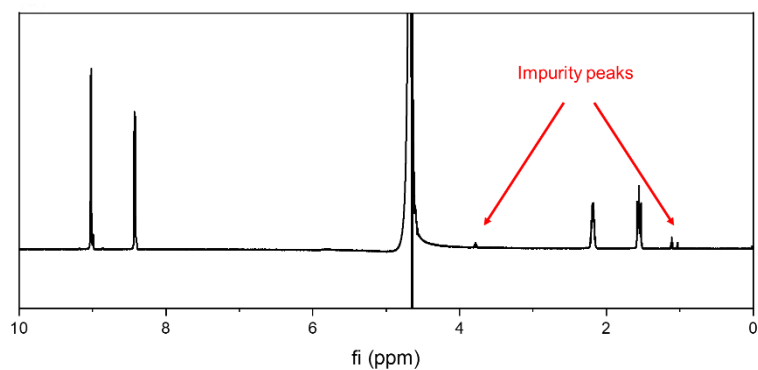


Figure S15. The ^1H NMR spectra of BPPV in D_2O . The hydrogen peaks of possible impurity were shown at the H (δ 3.79, 1.11, and 1.03).

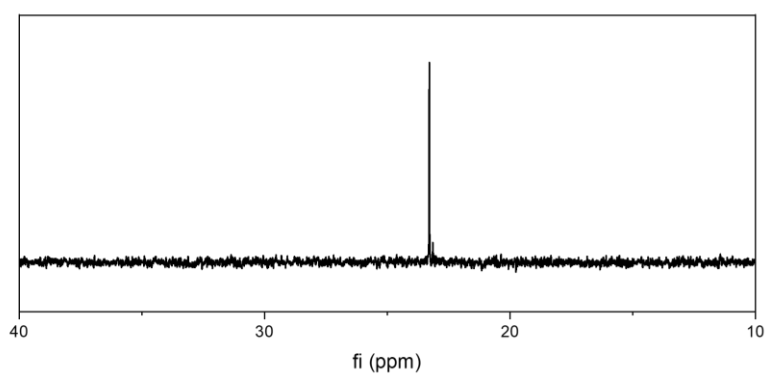


Figure S16. The ^3P NMR spectra of BPPV in D_2O . A single phosphoric peak ($-\text{PO}_3$) was shown at the P (δ 23.26).

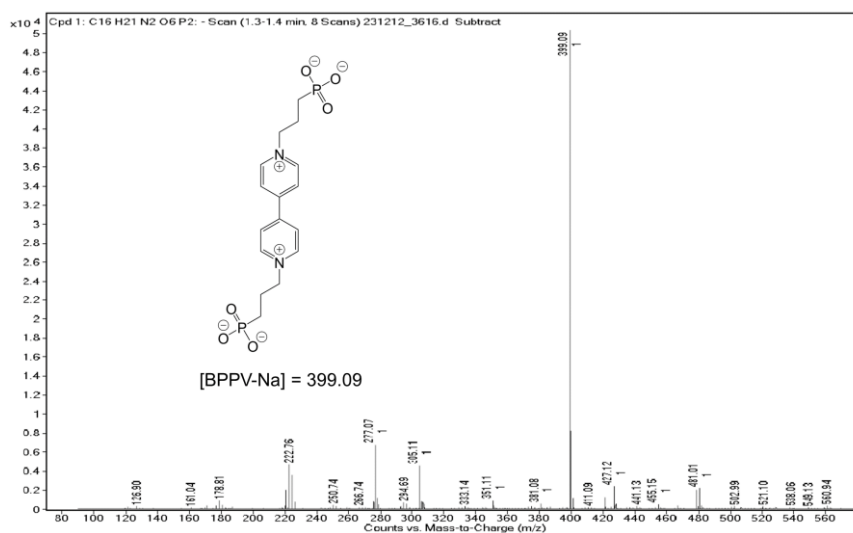


Figure S17. The high-resolution mass spectrometry profile of BPPV. The m/z of calculated $\text{C}_{16}\text{H}_{21}\text{N}_2\text{O}_6\text{P}_2$ (BPPV-Na): 399.09.

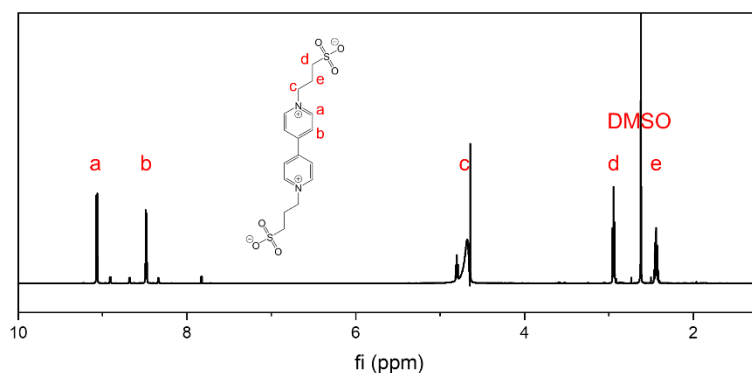


Figure S18. The ^1H NMR spectra of SPRV in DMSO reveals distinct peaks, with the DMSO solvent peak positioned at 2.6 ppm. The labels correlate individual peaks to specific chemical bonds.

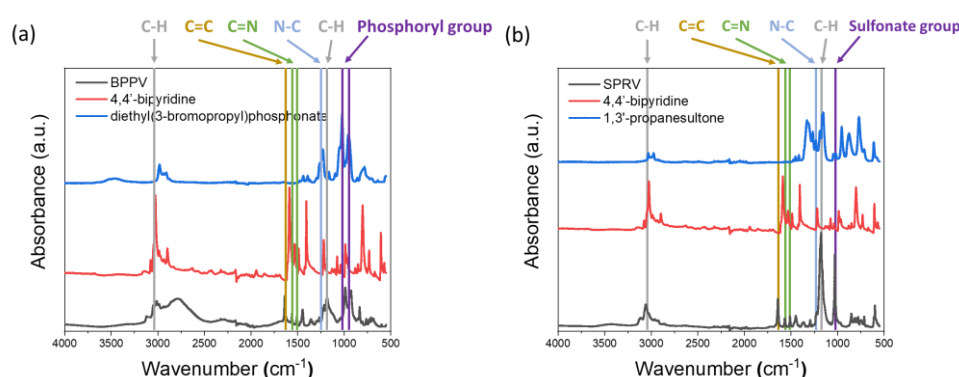


Figure S19. The Fourier-transform infrared spectroscopy (FT-IR) analysis of: (a) BPPV, 4,4'-bipyridine, and diethyl(3-bromopropyl)phosphonate, (b) SPRV, 4,4'-bipyridine, and 1,3'-propanesultone. As shown in the FT-IR results, the peak at 1637 cm^{-1} is the stretching of the C=C bond, and the peaks at 1180 and 3027 cm^{-1} are the stretching of the C-H bond. N-C stretching appears at 1216 cm^{-1} . The peaks at 1508 and 1561 cm^{-1} are from C=N vibration, while 947 and 1030 cm^{-1} are the vibrational peaks of the phosphoryl group. 1030 cm^{-1} is the vibrational peak of the sulfonate group.

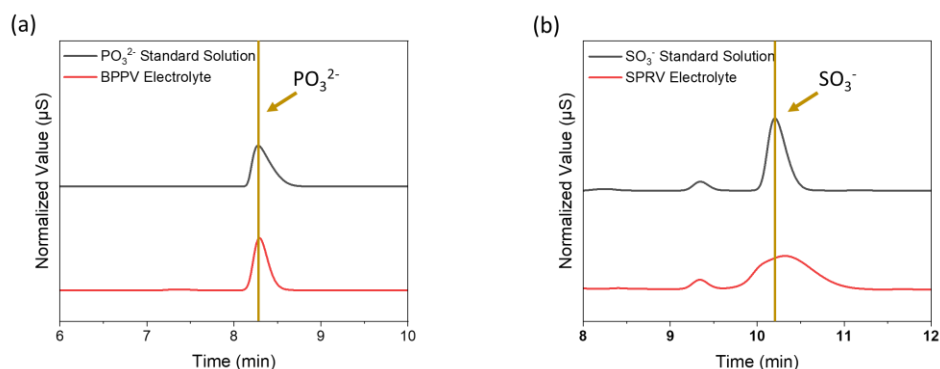


Figure S20. The high-pressure ion chromatography (IC) analysis of standard samples, BPPV and SPRV: (a) 0.5 mM PO_3^{2-} standard solution; 0.5 mM BPPV electrolyte, (b) 0.5 mM SO_3^- standard solution; 0.5 mM SPRV electrolyte. As shown in the IC results, the phosphoryl group appears at 8.3 mins and the

sulfonate group appears at 10.2 mins.

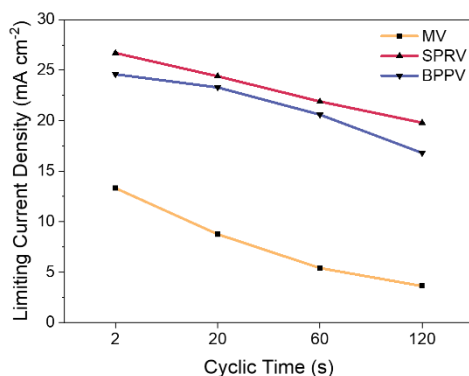


Figure S21. Limiting current densities of 0.1 M MV, SPRV, and BPPV in 1 M NaCl aqueous electrolyte during two-electrolyser CVE operation with different cycle periods.

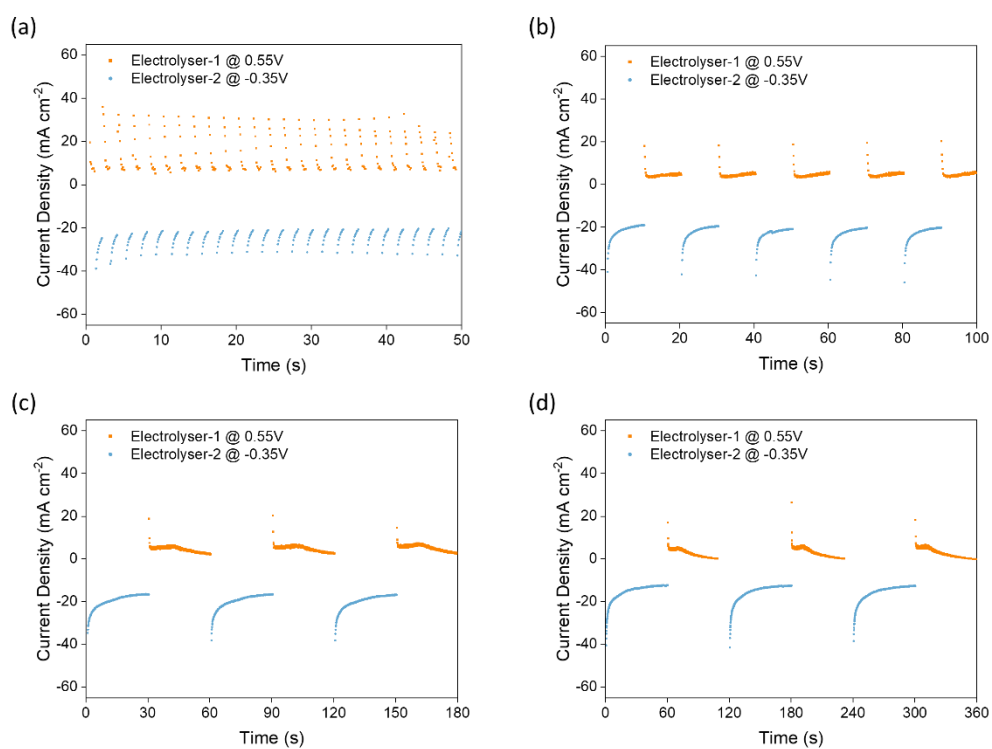


Figure S22. Performance using 0.1 M MV in 1 M NaCl aqueous electrolyte during two-electrolyser CVE operation with different cycle periods: (a) 2 s, (b) 20 s, (c) 60 s, (d) 120 s.

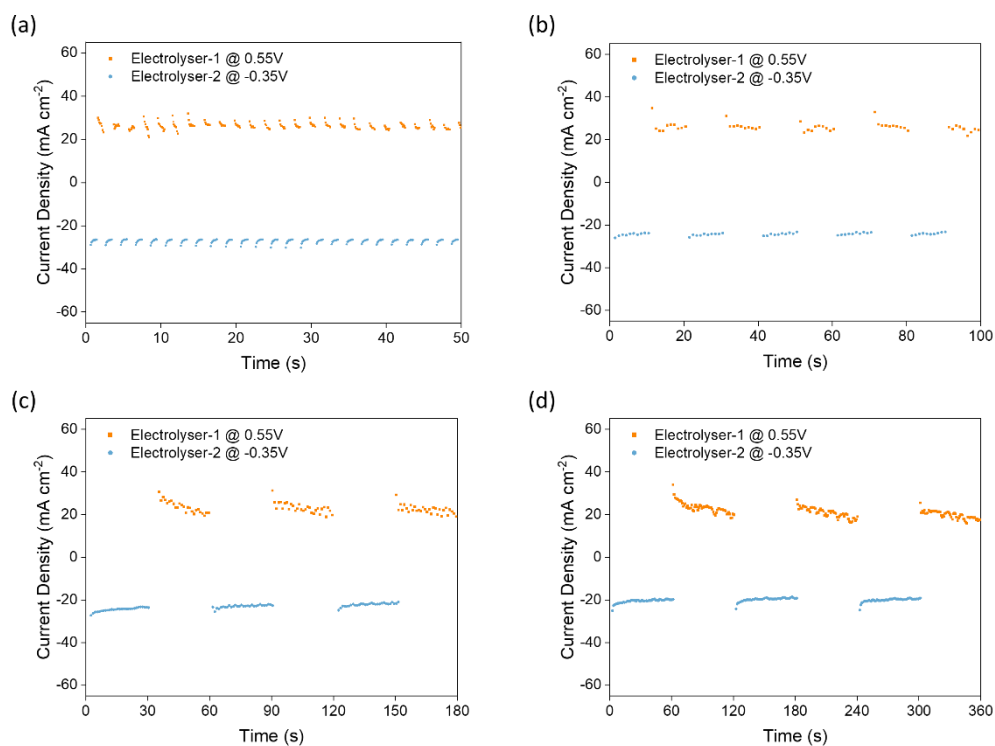


Figure S23. Performance using 0.1 M SPRV in 1 M NaCl aqueous electrolyte during two-electrolyser CVE operation with different cycle periods: (a) 2 s, (b) 20 s, (c) 60 s, (d) 120 s.

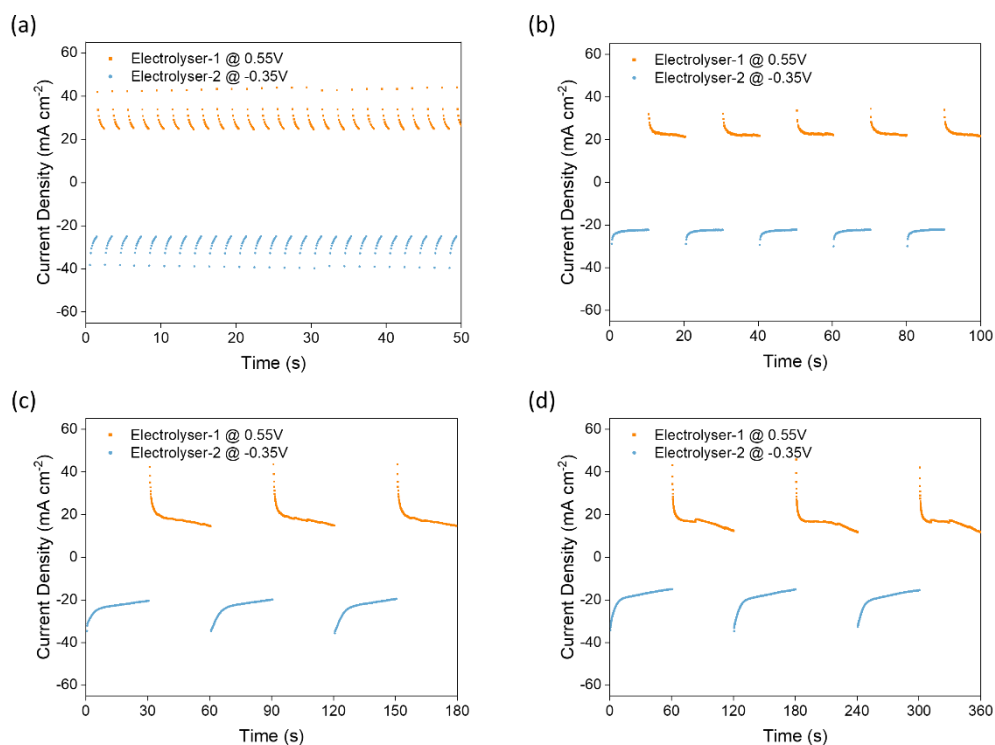


Figure S24. Performance using 0.1 M BPPV in 1 M NaCl aqueous electrolyte during two-electrolyser CVE operation with different cycle periods: (a) 2 s, (b) 20 s, (c) 60 s, (d) 120 s.

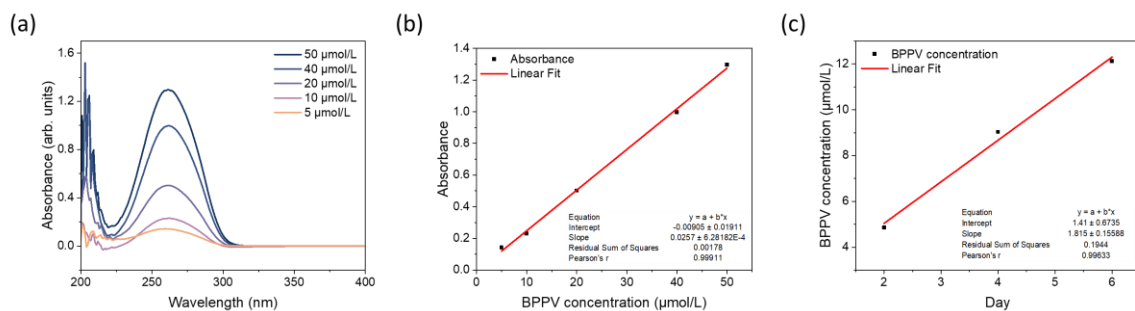


Figure S25. The UV-visible spectrophotometry (UV-vis) analysis for BPPV permeability: (a) UV-vis spectra of different BPPV concentrations, 5, 10, 20, 40, 50 μmol/L, (b) Calibration line from measured BPPV concentrations, (c) Estimated BPPV concentration in receiving compartment after 2, 4, and 6 days. The permeability of BPPV is $2.63 \times 10^{-11} \text{ cm}^2 \text{ s}^{-1}$. Details can be found in the “BPPV and SPRV permeability experiments” section.

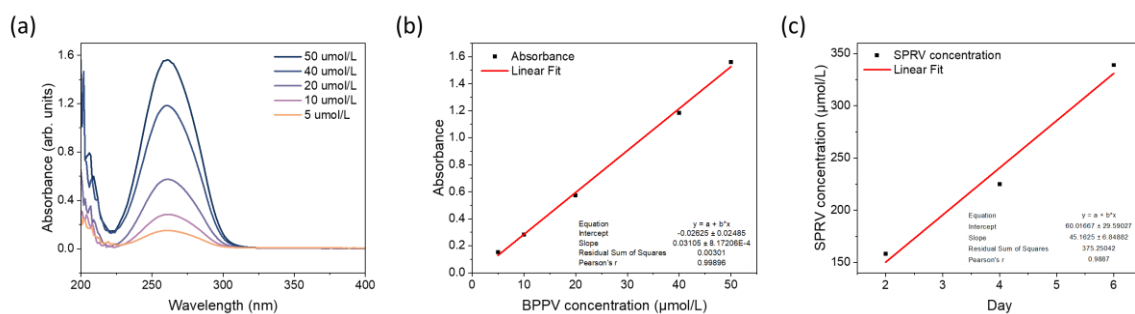


Figure S26. The UV-vis spectrophotometry analysis for SPRV permeability: (a) UV-vis spectra of different SPRV concentrations, 5, 10, 20, 40, 50 μmol/L, (b) Calibration line from measured SPRV concentrations, (c) Estimated SPRV concentration in receiving compartment after 2, 4, and 6 days. The permeability of SPRV is $7.37 \times 10^{-10} \text{ cm}^2 \text{ s}^{-1}$. Details can be found in the “BPPV and SPRV permeability experiments” section.

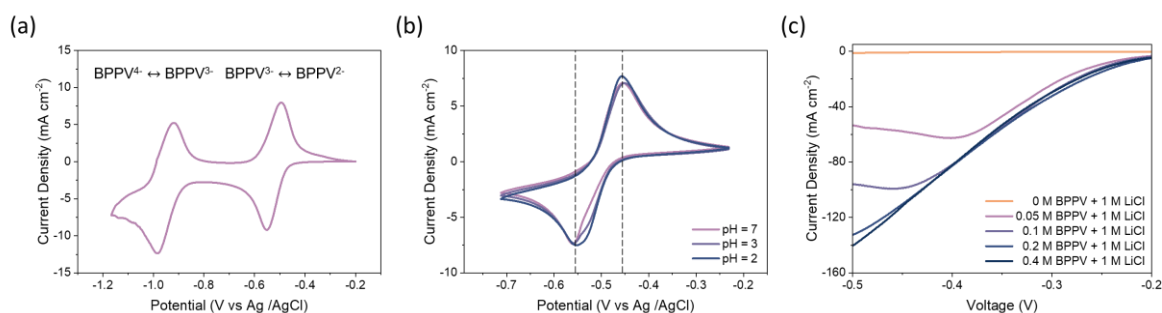


Figure S27. Electrochemical properties of BPPV. (a) Cyclic voltammograms of two electron transfer redox pairs of 0.02 M BPPV in 1 M NaCl aqueous electrolyte (H-cell configuration). (b) Cyclic voltammograms of 0.02 M BPPV in 1 M NaCl aqueous electrolyte in different electrolyte pH values (H-cell configuration). The pH was adjusted using hydrochloric acid. (c) Linear scan voltammetry of E2

with various BPPV concentrations in 1 M LiCl aqueous electrolyte (two-electrolyser CVE configuration).

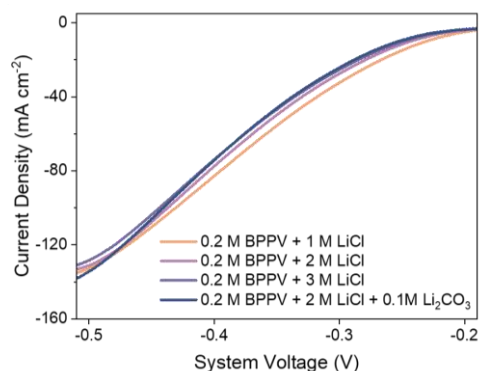


Figure S28. Linear scan voltammetry studies of the two-electrolyser CVE system using 0.2 M BPPV with different lithium concentrations and additional **0.1 M** carbonate salt.

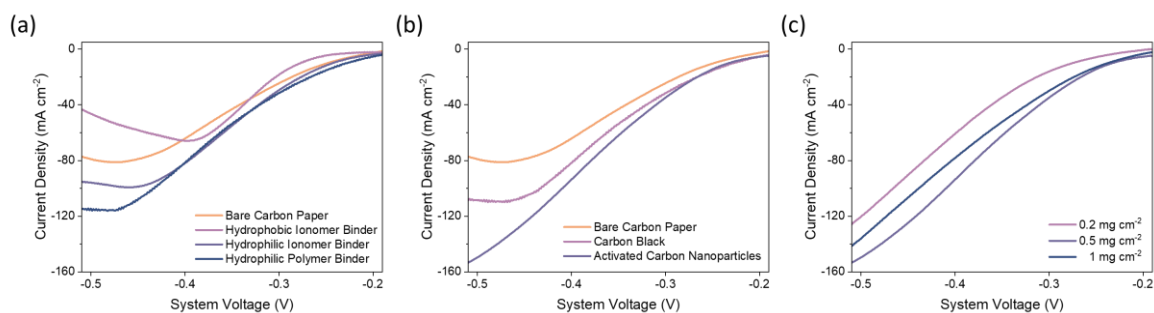
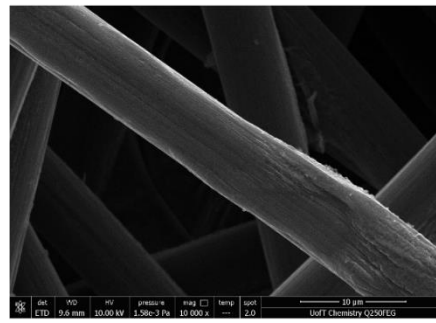
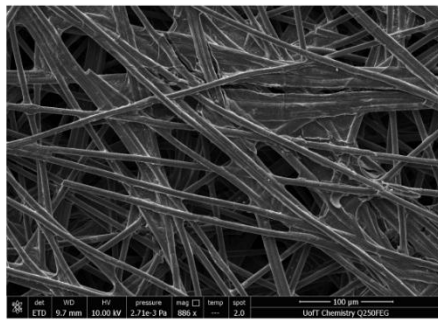


Figure S29. Linear scan voltammetry studies of the two-electrolyser CVE system using 0.1 M BPPV in 1 M LiCl with assorted electrode variations: (a) Catalyst binder comparison (with carbon black), (b) Catalyst material comparison (with hydrophilic polymer binder), (c) Catalyst loading comparison (activated porous carbon nanoparticle with hydrophilic polymer binder).

(a)



(b)

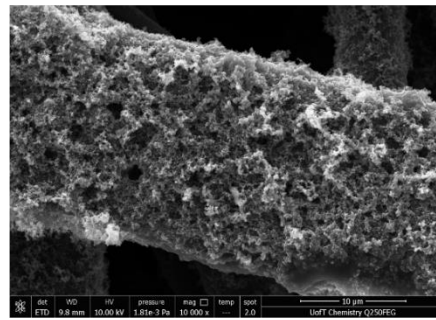
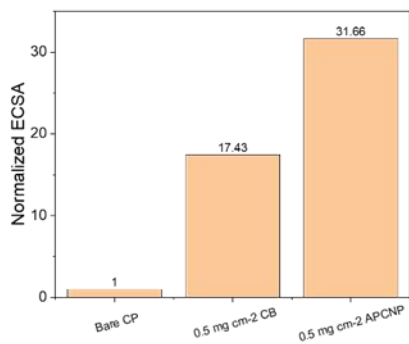
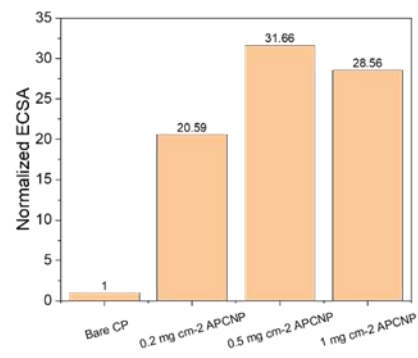


Figure S30. Scanning electron microscopy (SEM) imaging of the carbon electrode with the scale bar of 10 μm and 100 μm : (a) Bare carbon electrode, (b) Activated porous carbon nanoparticle coated carbon electrode.

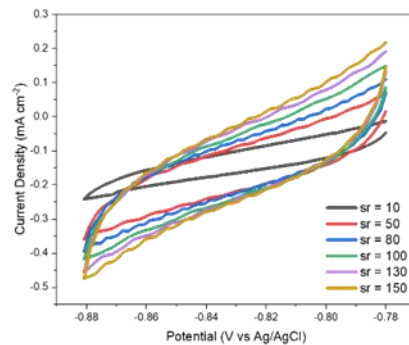
(a)



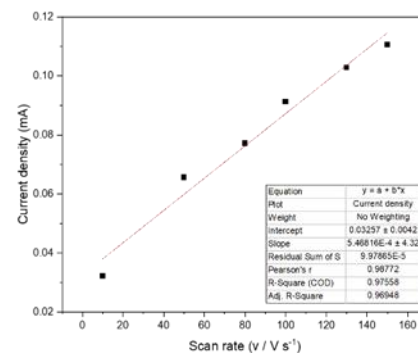
(b)



(c)



(d)



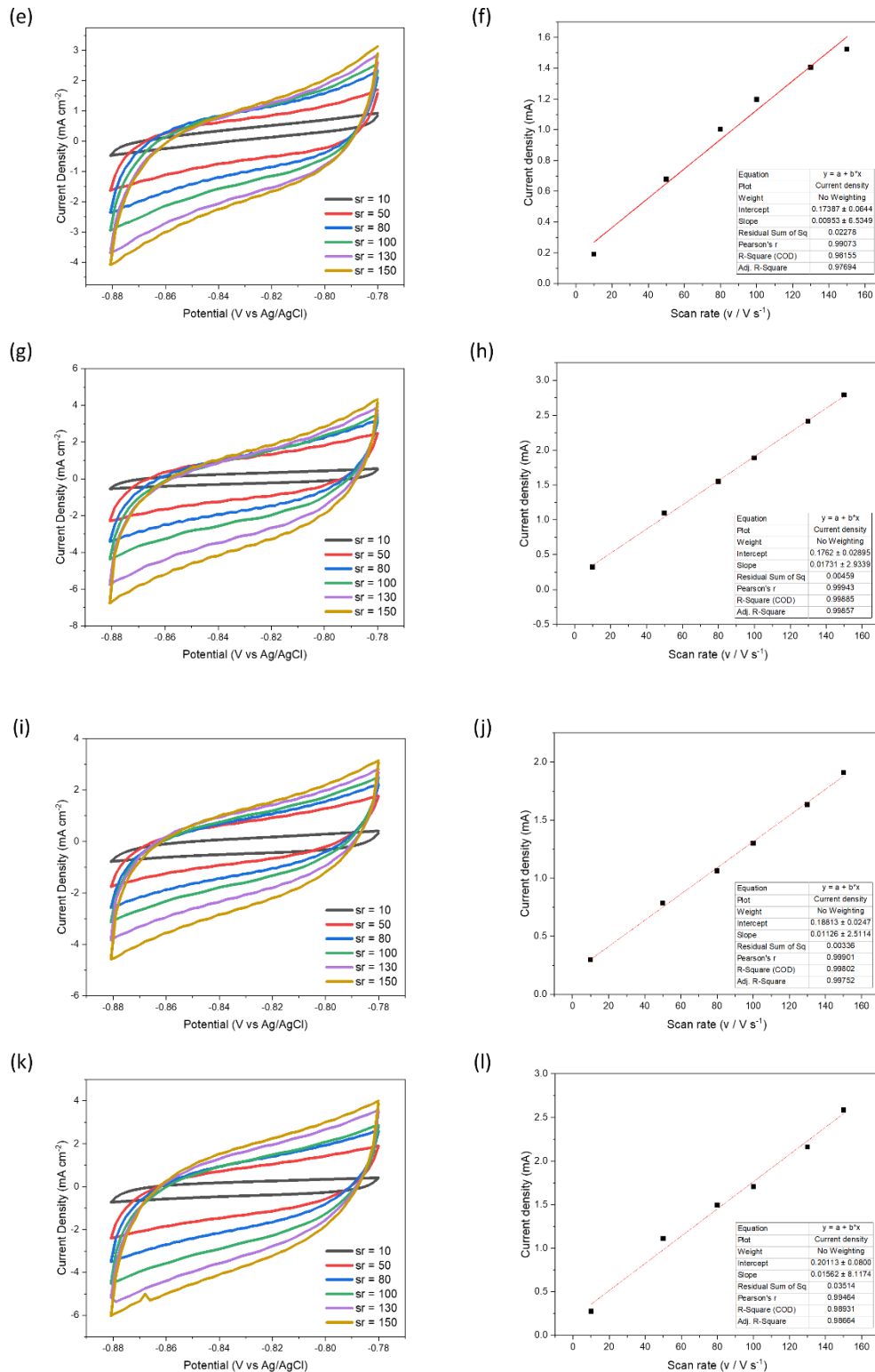


Figure S31. Electrochemically active surface area measurement in the H-cell configuration, using 1M NaCl aqueous electrolyte: (a) Summary of normalized ECSA results of bare carbon electrode, 0.5 mg cm⁻² CB-coated carbon electrode, 0.5 mg cm⁻² APCNP-coated carbon electrode; (b) Summary of normalized ECSA results of APCNP-coated carbon electrode of 0.2, 0.5, and 1 mg cm⁻² APCNP-coated carbon electrode; (c, d) ECSA result of bare carbon electrode; (e, f) ECSA result of 0.5 mg cm⁻² CB-

coated carbon electrode; (g, h) ECSA result of 0.5 mg cm^{-2} APCNP-coated carbon electrode; (i, j) ECSA result of 0.2 mg cm^{-2} APCNP-coated carbon electrode; (k, l) ECSA result of 1 mg cm^{-2} APCNP-coated carbon electrode. Details can be found in the “Electrochemically active surface area analysis:” section.

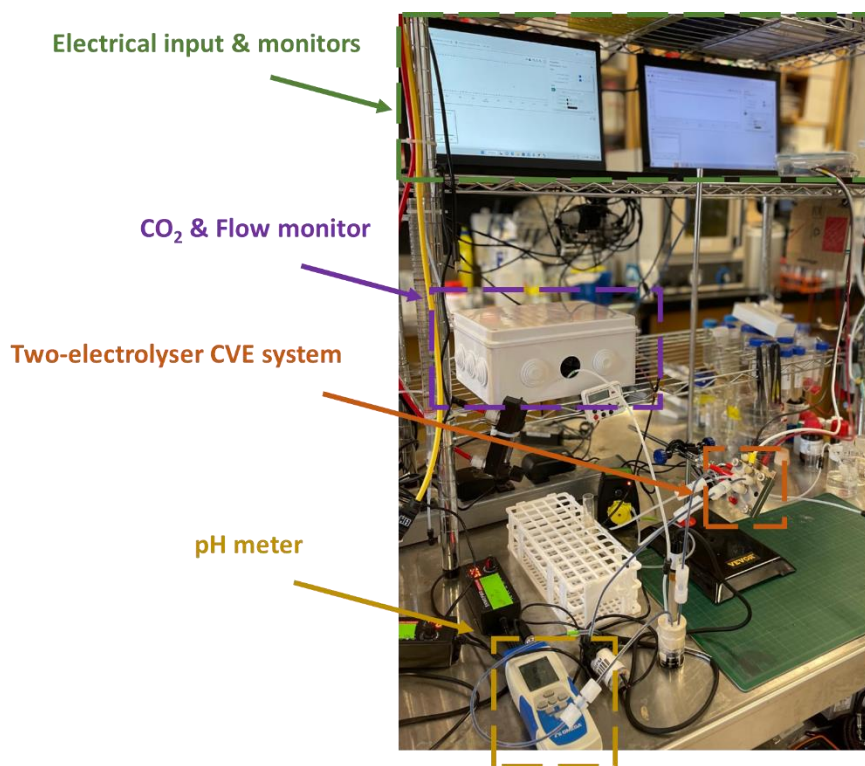


Figure S32. Experimental setup for two-electrolyser CVE operation.

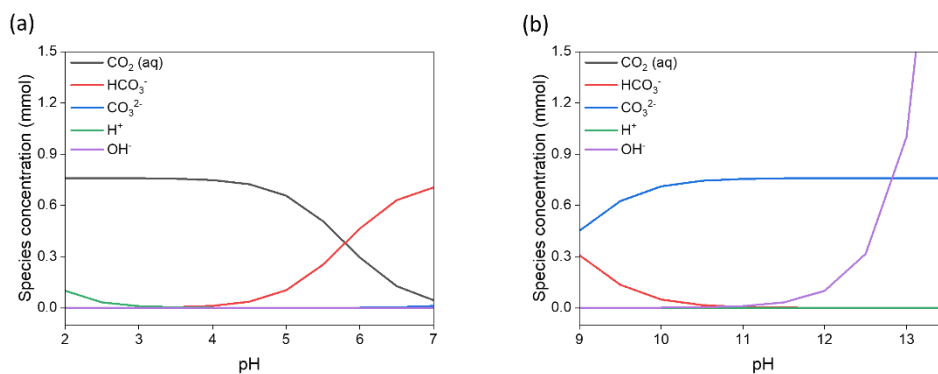


Figure S33. The modelled species concentrations in: (a) common electrolyte, (b) capture solution. Details can be found in the “Theoretical CO_2 capture and release analysis” section.

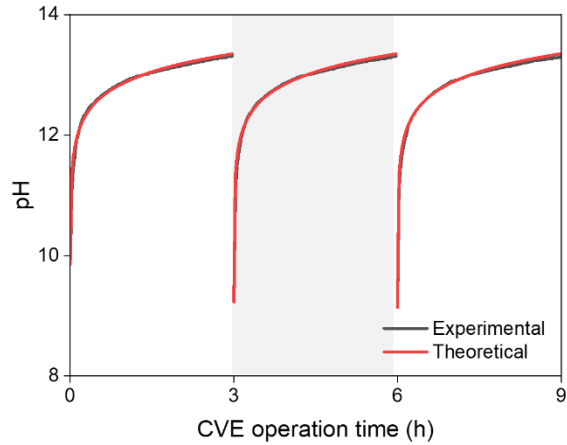


Figure S34. Theoretical and experimental capture solution pH. Details can be found in the “pH vs current calculation” section.

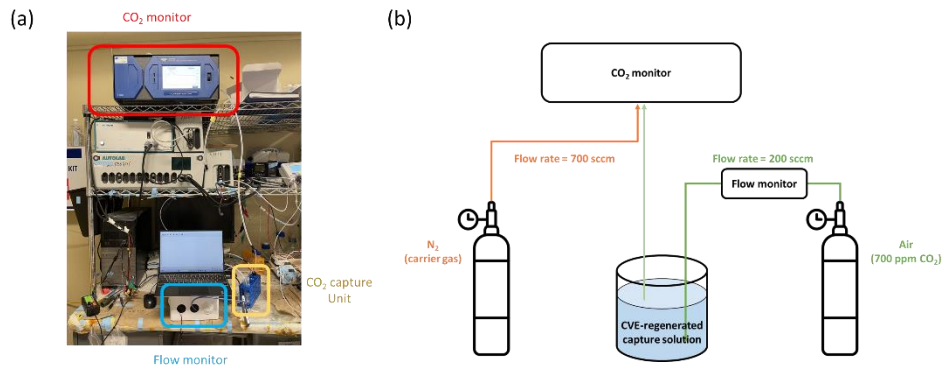


Figure S35. Experimental setup for DAC capture experiment with CVE-regenerated capture solution: (a) Image of setup for DAC capture experiment, (b) Schematic of setup for DAC capture experiment. Details can be found in the “Direct air capture experiment” section.

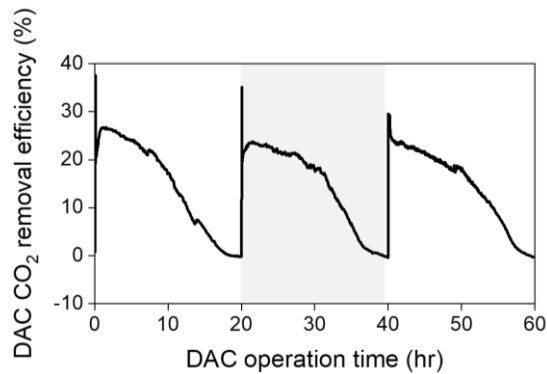


Figure S36. Experimental results of DAC capture experiments with CVE-regenerated capture solution: DAC CO₂ removal efficiency, Details can be found in the “Direct air capture experiment” section.

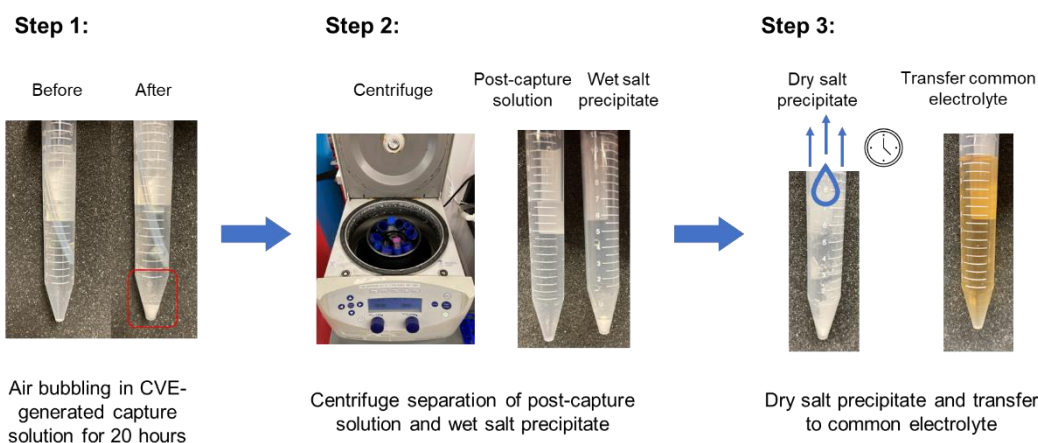


Figure S37. Experimental demonstration of Li_2CO_3 precipitate & transfer process: Step 1: air bubbling in CVE-capture solution (before) to form Li_2CO_3 salt precipitate (after); step 2: centrifugation to separate the Li_2CO_3 salt precipitate from the post-capture solution; step 3: dry salt precipitate was formed and mixed with the common electrolyte (precipitate transfer efficiency: $93.1 \pm 1.9\%$).

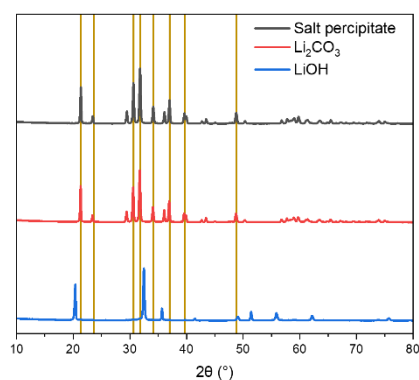


Figure S38. XRD measurement of salt precipitate, Li_2CO_3 , and LiOH chemical

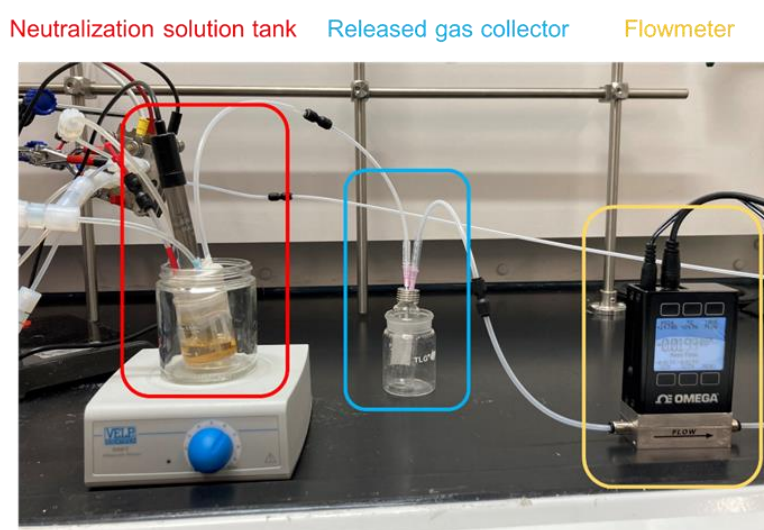


Figure S39. Experimental setup for CO_2 release experiments with Li_2CO_3 mixed common electrolyte. Details can be found in the “ CO_2 release analysis” section.

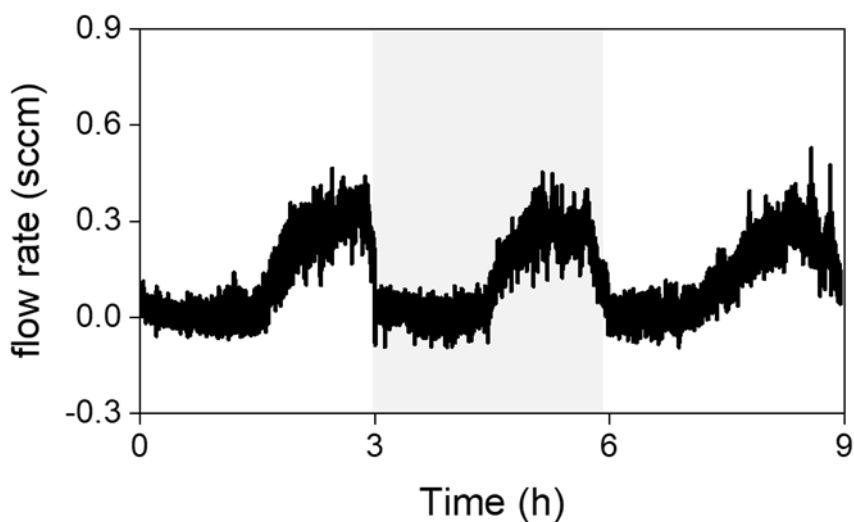


Figure S40. Experimental results of CO₂ release experiments with Li₂CO₃ mixed common electrolyte: flow rate of total gas released from neutralization solution tank. Details can be found in the “CO₂ release analysis” section.

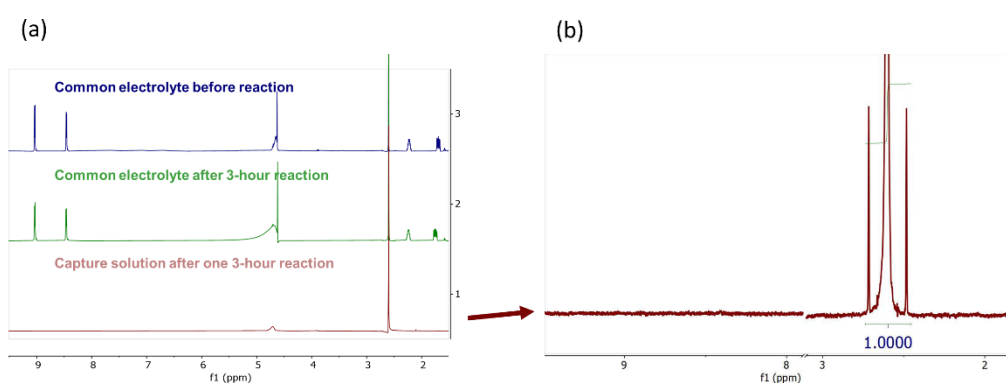


Figure S41. ¹H NMR spectra of capture and common electrolyte: (a) Before and after 1 round (3-hour) reaction in DMSO, (b) Quantification of BPPV in capture solution (pH 13.3) after 1 round of operation.

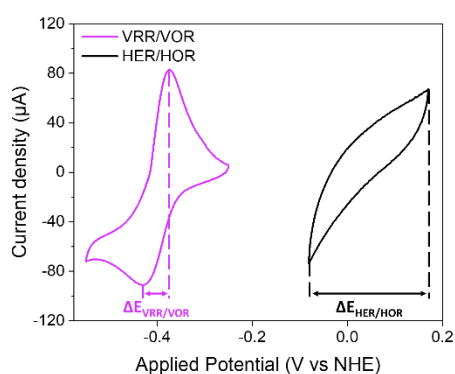


Figure S42. Cyclic voltammetry of DI water and diluted BPPV solution at room temperature

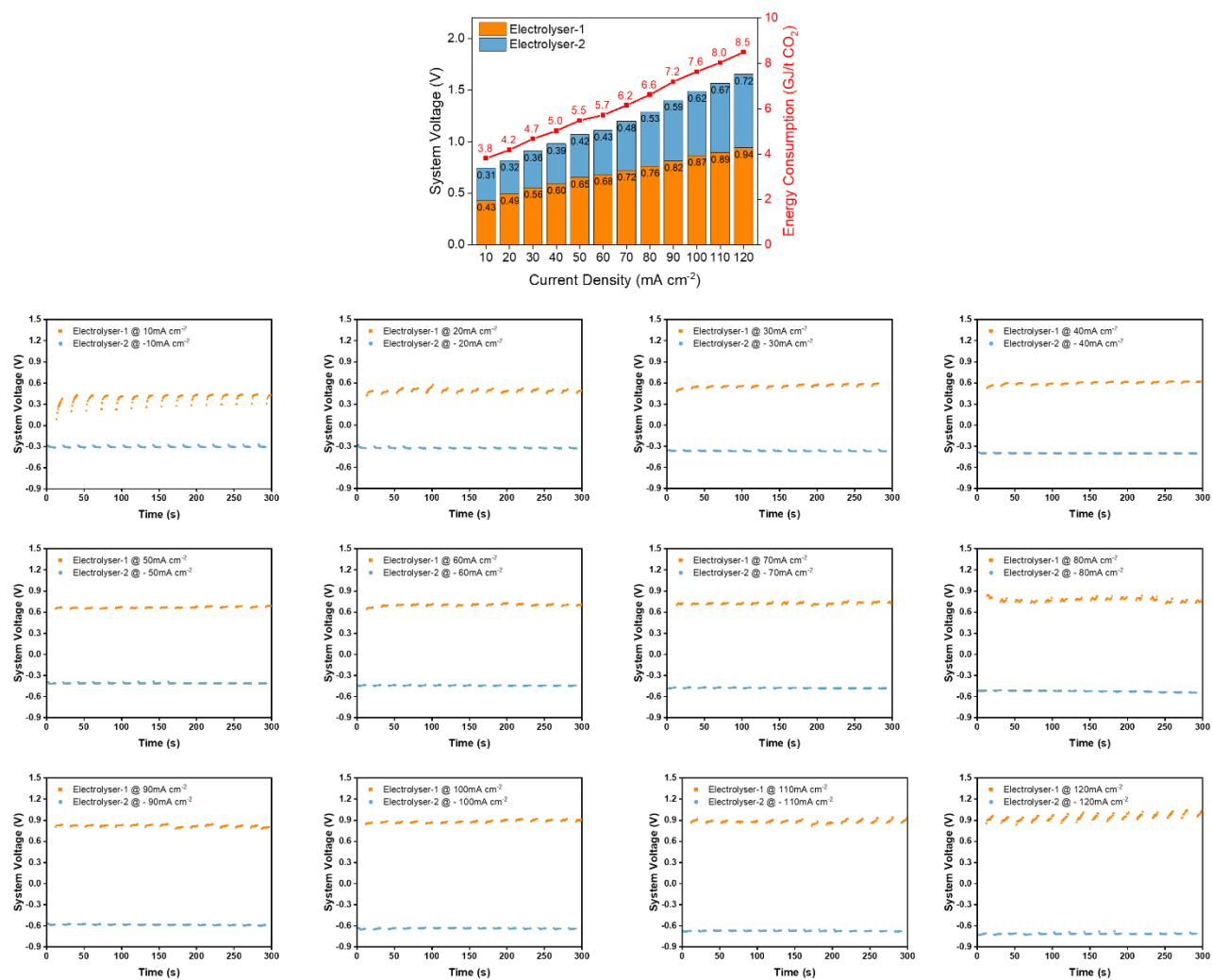


Figure S43. Two-electrolyser CVE voltage and energy consumption at current densities of 10 – 120 mA cm⁻².

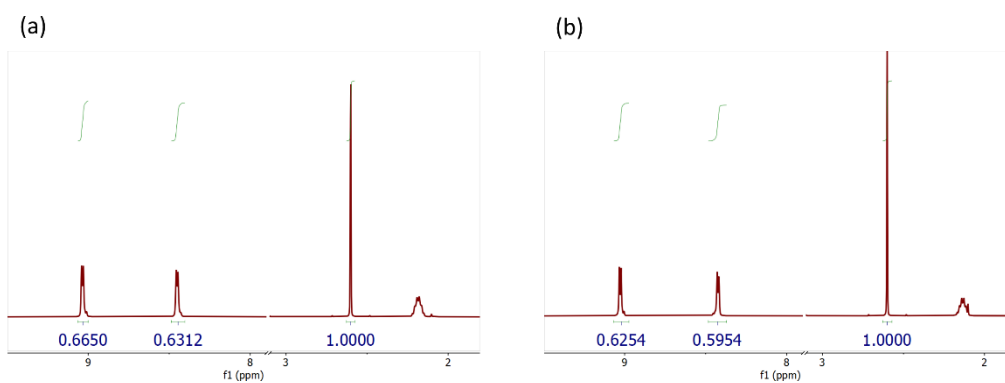


Figure S44. ¹H NMR spectra of common electrolyte (in DMSO solvent): (a) before, (b) and after 200 hours (67 rounds) of reaction.

DFT method:

DFT was applied to explore the interactions between the viologen molecules and the carbon (graphene) electrode. All DFT calculations were carried out in the Vienna ab initio simulation package with a plane wave pseudo-potential implementation.¹⁻⁴ The exchange-correlation functional was described by the spin-polarized generalized gradient approximation of Perdew-Burker-Ernzerhof and the electron-ion interactions were described by projector augmented wave potentials.^{3,5,6} The kinetic cut-off energy of 450 eV was used for the plane-wave expansion. The $3 \times 3 \times 1$ Monkhorst-Pack k-point mesh was used for geometry optimization, with the convergence criteria of electronic and ionic iterations being 10^{-5} eV and $0.02 \text{ eV } \text{\AA}^{-1}$, respectively.⁷ The long-range Van de Waals interactions were described by the zero-damping DFT - D3 method of Grimme et al.⁸ An 8×8 supercell of graphene with 128 atoms was applied as the carbon substrate. Viologen molecules, including methyl-substituted viologen (MV), 1,1'-bis(3-sulfonatopropyl)-4,4'-bipyridinium (SPRV), 1,1'-bis(3-phosphonopropyl)-4,4'-bipyridinium (BPPV), benzyl-substituted viologen (BV), bis(2-phosphono-methyl-4-benzyl)-4,4'-bipyridinium (BNV), 1,1'-bis(2-(1h-indol-3-yl)ethyl)-4,4'-bipyridinium (IEV), and (1-H-Phenalene-5-yl)methyl-4,4'-bipyridinium (PMV), were then placed on the carbon surface for geometry optimization to explore their interactions. A 15 \AA vacuum space was set among the periodic surfaces in the z-direction to decouple the interaction between them. Note that, the side chain of SPRV, BPPV, BNV molecules carries charges of -1, -2, and -2, respectively. To avoid the intricacies arising from net charges during DFT calculation, protons were applied to neutralize these side chains, i.e. adding 1, 2, and 2 protons to the side chains of SPRV, BPPV, and BNV, respectively, in accordance with their respective charges.

The binding strength of viologen molecules on the carbon electrode was evaluated by calculating their binding energies as (E1):

$$E_b = E_a - (E_s + E_m) \quad (\text{E1})$$

where E_a , E_s , and E_m are the energies of an adsorbed system, bare carbon surface, and isolated

viologen molecules, respectively.

In this study, different possible conformations of the viologen molecules (Fig. S3, ESI[†]) were calculated. Additionally, multiple binding configurations of each viologen molecule on carbon electrode were examined (Fig. S4-S11, ESI[†]).

Synthesis of di-polar viologens:

Synthesis of 1,1'-bis[2-sulfonatopropyl]-4,4'-bipyridinium (SPRV):

1.57 grams of 1,3'-propanesultone and 1 gram of 4,4'-bipyridine were mixed with 20 millilitres of toluene. The reaction took place on a heating plate set to 110°C and was stirred for 4 hours under a nitrogen atmosphere. The resulting slurry was subjected to five cycles of washing with acetonitrile before being centrifuged. The resulting white solid, SPRV, was dried under vacuum for 24 hours.

Synthesis of 1,1'-bis(3-phosphonopropyl)-[4,4'-bipyridine]-1,1'-dium dibromide (BPPV):

1.36 grams of 4,4'-bipyridine and 5 millilitres of diethyl(3-bromopropyl)phosphonate were mixed with 20 millilitres of dimethylformamide. The reaction took place on a heating plate set to 95°C and was stirred for 72 hours under a nitrogen atmosphere. The resulting slurry was subjected to five cycles of washing with acetonitrile before being centrifuged. The resulting pink-white solids, 1,1'-bis(3-(diethoxyphosphoryl)propyl)-[4,4'-bipyridine]-1,1'-dium dibromide, were dried under vacuum for 24 hours.

0.674 grams of 1,1'-bis(3-(diethoxyphosphoryl)propyl)-[4,4'-bipyridine]-1,1'-dium dibromide and 1.32 millilitres of bromotrimethylsilane were mixed with 12 millilitres of dichloromethane. The reaction was carried out at room temperature and stirred for 24 hours under a nitrogen atmosphere. The resulting orange solution was washed five times with isopropyl alcohol before being centrifuged. The resulting orange-white solid, BPPV, was then dried under vacuum for 24 hours.

BPPV purity analysis:

To assess and quantify the purity of the BPPV, additional characterizations were conducted, including ^1H NMR, ^1P NMR, and Mass spectrometry. In the mass spectrometry, the intensity of peaks other than the main peak at 399.09 m/z were negligible (Fig. S17, ESI⁺). The ^1P NMR revealed a single peak corresponding to $-\text{PO}_3$, which eliminating the possibility of other phosphoric containing precursor residual impurities (Fig. S16, ESI⁺). The hydrogen ratio calculated from ^1H NMR, H (δ 9.16, 8.60, 2.34-2.45, 2.02-2.12) is 1:1:1:1, consistent with the molecule formula of BPPV. This analysis also suggests that any impurities present from precursor residuals are minimal (Fig. S15, ESI⁺).

To quantify BPPV purity, we integrated the other hydrogen peaks H (δ 3.79, 1.11, and 1.03), which collectively account for less than 5% compared to the peak at δ 9.16. Considering that impurities typically involve more than one hydrogen atom, The BPPV purity exceeds 95%.

BPPV and SPRV permeability experiments:

The permeability of BPPV and SPRV was measured across a Nafion 115 cation exchange membrane. An H-cell configuration was employed, consisting of a donating compartment, with the viologen molecules, and a receiving compartment.

The donating compartment was filled with a solution containing 0.1 M SPRV or 0.1 M BPPV, while the receiving compartment was filled with DI water. Both compartments initially contained 10 mL of solution. To simulate the fluid convection present in the two-electrolyser CVE configuration, the experiments were placed with magnetic stir bars.

The migration of the viologen molecules were tracked over a period of 6 days with measurements taken from the receiving compartment every 2 days: 0.5 mL sample was removed from the receiving compartment. This withdrawn sample was subsequently diluted and analysed using UV-visible spectrophotometry to determine the viologen concentration.

The permeability of BPPV and SRPV was estimated using Fick's Law (E2):

$$P = \frac{\Delta \ln \left(1 - \frac{2C_i}{C_0} \right) \left(\frac{V_0 L}{2A} \right)}{\Delta t} \quad (E2)$$

Where P is the permeability ($\text{cm}^2 \text{s}^{-1}$), C_i is the viologen concentration measured in the receiving compartment, C_0 is the initial concentration of viologen in the donating compartment (0.1 M), V_0 is the initial volume of solution (10 mL), A is the effective membrane surface area (1.13 cm^2), L is the thickness of the membrane (0.0127 cm), and Δt is the time interval (s).

Electrochemically active surface area analysis:

The electrochemically active surface area of carbon electrodes was determined by assessing the electrochemical double-layer capacitance of the catalytic surface area.⁹ To achieve this, cyclic voltammetry (CV) was conducted at different scan rates, measuring the non-Faradaic capacitive current that corresponded to the charge of the double-layer.

To measure the ECSA, a potential range of -0.78 V to -0.88 V vs Ag AgCl⁻¹ was chosen, which no apparent Faradic processes occurred. All measured current in this potential range was assumed to be due to double-layer charging. The electrochemical double-layer capacitance was estimated using (E3):

$$C_{DL} = \frac{i_c}{\nu} \quad (E3)$$

Where C_{DL} is the electrochemical double-layer capacitance of the catalytic surface area, i_c is the charging current at different scan rates (mA), ν is the scan rate of the CV measurement (V s^{-1}).

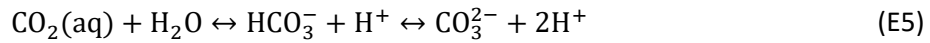
The ECSA of a carbon electrode was determined using (E4):

$$ECSA = \frac{C_{DL}}{C_s} \quad (E4)$$

Where C_s is the specific capacitance of the baseline sample (Bare carbon electrode).

Theoretical CO₂ capture and release analysis:

In alkaline capture liquids, the CO₂ was stored as dissolved inorganic carbon (DIC) in three primary forms: CO₂ (aq), bicarbonate (HCO₃⁻), and carbonate (CO₃²⁻). The equilibria presented in aqueous solution (E5):



The first and second stoichiometric equilibrium constants are K_1 and K_2 , respectively, and defined as following (E6), (E7):

$$K_1 = \frac{[\text{HCO}_3^-][\text{H}^+]}{[\text{CO}_2(\text{aq})]} \quad (\text{E6})$$

$$K_2 = \frac{[\text{CO}_3^{2-}][\text{H}^+]}{[\text{HCO}_3^-]} \quad (\text{E7})$$

The values for K_1 and K_2 are 1.543×10^{-6} M ($\text{p}K_1 = 5.81$) and 1.437×10^{-9} M ($\text{p}K_2 = 8.84$), respectively.¹⁰ When $\text{pH} < 5.81$, total DIC is presented as primarily CO₂ (aq), in the intermediate region of $5.81 < \text{pH} < 8.84$, the total DIC is presented as primarily of HCO₃⁻, and when $\text{pH} > 8.84$, the total DIC is presented as primarily of CO₃²⁻.

The concentration of hydroxide and proton can be considered from water dissociation (E8):



The equilibrium constant for water dissociation K_w is 10^{-14} M².

The sum of the DIC species present in solution (E9):

$$\text{DIC} = [\text{CO}_2(\text{aq})] + [\text{HCO}_3^-] + [\text{CO}_3^{2-}] \quad (\text{E9})$$

The total alkalinity (TA) of solution can be defined as (E10):

$$TA = [\text{HCO}_3^-] + 2[\text{CO}_3^{2-}] + [\text{OH}^-] - [\text{H}^+] \quad (\text{E10})$$

The aqueous CO₂ concentration can be obtained based on the Henry's Law (E11):

$$[\text{CO}_2(\text{aq})] = K_H * P_{\text{CO}_2} \quad (\text{E11})$$

The relationship of equilibrium TA and DIC at atmospheric condition can be expressed as¹¹ (E12):

$$\text{DIC} = 0.53 \times \text{TA} \quad (\text{E12})$$

During the theoretical consideration, the concentration of CO₂ (aq), HCO₃⁻, and CO₃²⁻ can be estimated as a function of pH via the following equations (E13) - (E15):

$$[\text{CO}_2(\text{aq})] = \frac{\text{DIC}}{1 + \frac{K_1}{[\text{H}^+]} + \frac{K_1 K_2}{[\text{H}^+]^2}} \quad (\text{E13})$$

$$[\text{HCO}_3^-] = \frac{\text{DIC}}{1 + \frac{[\text{H}^+]}{K_1} + \frac{K_2}{[\text{H}^+]}} \quad (\text{E14})$$

$$[\text{CO}_3^{2-}] = \frac{\text{DIC}}{1 + \frac{[\text{H}^+]}{K_2} + \frac{[\text{H}^+]^2}{K_1 K_2}} \quad (\text{E15})$$

pH vs. current calculation:

Faraday's law was applied to calculate the production rate (in mol s⁻¹) of OH⁻ and H⁺ in the capture solution and regeneration solutions, respectively (E16), (E17):

$$r_{\text{OH}^-} = \frac{I_{\text{electrolysis 1}}}{2 * nF} \quad (\text{E16})$$

$$r_{\text{H}^+} = \frac{I_{\text{electrolysis 2}}}{2 * nF} \quad (\text{E17})$$

Where $I_{electrolysis\ 1\ \&\ 2}$ represents the applied current for electrolyser-1 and electrolyser-2, n is the number of electrons transferred per hydroxide or proton ($n=1$), F is Faraday's constant ($96485\ \text{s A mol}^{-1}$). The production rates were halved because each electrolyzer was operated for half the time. Since electrolyser-1 and electrolyser-2 are operated at the same current density, $r_{OH^-} = r_{H^+}$.

Direct air capture experiment:

The CVE-regenerated capture solution (10 mL, initial pH of 13.3 ± 0.02) was employed for capturing CO_2 from air flowing at 200 sccm and a concentration of ~ 700 ppm, typical of an indoor/lab environment. The experimental setup for DAC experiment is detailed in (Fig. S35, ESI⁺). The air flow rate and CO_2 concentration were monitored using a flowmeter (Honeywell AWM3300V) and CO_2 monitor (Teledyne T360M), respectively. As the solution pH dropped below 11, the CO_2 capture rate rapidly declined, reaching approximately 0 ppm. This decline was attributed to the kinetic limitations imposed by the low concentration of CO_2 and OH^- ions required for bicarbonate formation. Considering both DIC and pH, we hypothesized that effectively all OH^- ions capture CO_2 , forming only CO_3^{2-} . This hypothesis is supported by the post-capture solution pH of 10.4 ± 0.3 and the representation of $> 99\%$ of DIC as CO_3^{2-} . (Fig. S33, ESI⁺).

Theoretical DAC capture:

The CVE-regenerated capture solution, starting with a pH of 13.3 ± 0.02 , transitions to a post-capture solution with a pH of 10.4 ± 0.3 . The total OH^- concentration consumed in the 10 mL capture solution equates to 2 ± 0.2 mmol, aligning with the anticipated capture of 1 ± 0.1 mmol CO_2 , given the 2:1 ratio of OH^- to CO_2 required to form carbonate.

The DAC CO_2 capture rate was calculated from the following equations (E18):

$$cCO_{2-captured} = (cCO_{2-surrounding} - cCO_{2-monitored}) \cdot \frac{f_{total}}{f_{air}} \quad \text{(E18)}$$

Where the $cCO_{2-captured}$ is the total DAC CO_2 concentration that captured by LiOH capture solution

(ppm). The $cCO_{2-surrounding}$ is the steady-state CO₂ concentration reading before employing the capture solution, representing the indoor environment (ppm). $cCO_{2-monitored}$ is the CO₂ concentration reading remaining in the outlet stream (ppm), which is monitored by the CO₂ monitor. The f_{total} is the total gas flow rate (N₂ carrier gas + air outlet), which is monitored by the CO₂ monitor (sccm). The f_{air} is the outlet stream of air (sccm), which monitored by the flowmeter.

The CO₂ removal efficiency was calculated from the following equation (E19):

$$\eta_{CO_2-removal} = \frac{cCO_{2-captured}}{cCO_{2-surrounding}} \quad (E19)$$

Where $\eta_{CO_2-removal}$ is the CO₂ removal efficiency (%).

The total amount of DAC CO₂ captured was calculated from the following equations (E20), (E21):

$$Q_{CO_2-captured} = (cCO_{2-captured}) \cdot f_{air} \quad (E20)$$

$$n_{CO_2-captured} = \frac{P \cdot Q_{CO_2-captured} \cdot t}{R \cdot T} \quad (E21)$$

Where $Q_{CO_2-captured}$ is the volumetric flow rate of CO₂ capture (mL min⁻¹), $n_{CO_2-captured}$ is the total amount of DAC CO₂ captured (mmol), t is the operation time (min), P is the atmospheric pressure (101325 pa), R is the gas constant (8.31 $\frac{J}{K \cdot mol}$), T is the atmospheric temperature (298 K).

CO₂ release analysis:

In the lab-scale Li₂CO₃ salt precipitate and transfer process, a total of 68.8 ± 1.4 mg of dry salt precipitate was transferred to the BPPV common electrolyte (10 mL), which corresponds to 0.93 ± 0.02 mmol of carbonate concentration initially in the neutralization solution tank. Gaseous CO₂ was released over the span of the 3-hour CVE experiment as protons continuously react with carbonate. The experimental setup for CO₂ release experiment is detailed in (Fig. S39, ESI). The released CO₂ gas flow rate was monitored by a flowmeter (Omega FMA-LP1615A) and the collected released gas

product was analysed by gas chromatography (PerkinElmer Clarus 680) at the end of the experiment.

Theoretical CO₂ release:

The released CO₂ gas purity was estimated assuming the outlet gas stream is CO₂ and H₂O vapor, and that both behave as ideal gases. The total pressure of CO₂ + H₂O was taken to be 101kPa (atmospheric pressure). The temperature of CO₂ release system was assumed to be 298K, at which the vapor pressure of water is 3.17 kPa. Assuming the outlet stream is 100% humidity, the outlet gas includes 96.9% CO₂ and 3.1% H₂O. When protons react with carbonates, 0.93 ± 0.02 mmol CO₂ is expected to be released since 1 CO₃²⁻ is neutralized into 1 CO₂.

The total amount of CO₂ released experimentally was calculated from the following equations (E22):

$$n_{CO_2-released} = \frac{P \cdot Q_{released} \cdot t}{R \cdot T} \cdot x_{CO_2} \quad (E22)$$

Where $Q_{released}$ is the volumetric flow rate of total outlet gas (mL min⁻¹), x_{CO_2} is the CO₂ molar concentration (97%), and $n_{CO_2-released}$ is the total amount of CO₂ released (mmol).

Minimum energy requirements:

The minimum energy requirement was calculated from the cyclic voltammetry analysis (E23), (E24):

$$\begin{aligned} E_{cell} &= E_{electrolysis-1} + E_{electrolysis-2} = (E_{HER} - E_{VOR}) + (E_{VRR} - E_{HOR}) \\ &= \Delta E_{HER/HOR} + \Delta E_{VRR/VOR} = 0.32 V \end{aligned} \quad (E23)$$

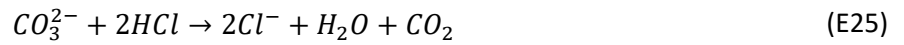
$$W_{CO_2} = \frac{(E_{cell}) \times 96.49 \text{ kJ/mol} \cdot eV}{\eta_{current} \times \eta_{precipitate\ transfer}} = 38.1 \frac{\text{kJ}}{\text{molCO}_2} = 0.82 \frac{\text{GJ}}{\text{tCO}_2} \quad (E24)$$

Where $\Delta E_{HER/HOR}$ represents the voltage difference between hydrogen reduction and oxidation peak (0.25 V, obtained from Fig. S42, ESI⁺), and $\Delta E_{VRR/VOR}$ represents the voltage difference between BPPV oxidation and reduction peak (0.07 V, obtained from Fig. S42, ESI⁺), W_{CO_2} is the work required to capture a specific mass of CO₂, $\eta_{current}$ is the average current efficiency of the CVE

system (92%), $\eta_{precipitate\ transfer}$ is the solid Li_2CO_3 salt precipitate transfer efficiency (93%).

Two-electrolyser CVE System Energy Consumptions (Carbonate):

Lithium carbonate post-capture solution required two hydroxides to capture one CO_2 molecule. Therefore, two electrons are needed to regenerate the hydroxide through the electrochemical process (E25). The energy consumption of the two-electrolyzer CVE system to capture 1 tonne of CO_2 was calculated (E26):

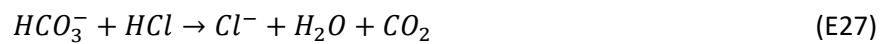


$$w_{\text{CO}_2} = \frac{W_{\text{CO}_2}}{m_{\text{CO}_2}} = \frac{2 \times F \times [(E_{E1} + E_{E2}) \times I_{\text{cell}}]}{I_{\text{cell}} \times M_{\text{CO}_2} \times \eta_{\text{current}} \times \eta_{\text{precipitate transfer}}} \quad (\text{E26})$$

Where E_{E1} and E_{E2} are the practical voltage required of electrolyser-1 and electrolyser-2 systems (obtained from Fig. S43, ESI[†]), I_{cell} is the CVE current density (obtained from Fig. S43, ESI[†]). M_{CO_2} is the CO_2 molar mas (44 g mol^{-1})

Two-electrolyser CVE System Energy Consumptions (Bicarbonate):

Lithium bicarbonate post-capture solution requires one hydroxide to capture one CO_2 molecule. Therefore, one electron is needed to regenerate the hydroxide through the electrochemical process (E27). The energy consumption of the two-electrolyzer CVE system to capture 1 tonne of CO_2 was calculated (E28):



$$w_{\text{CO}_2} = \frac{W_{\text{CO}_2}}{m_{\text{CO}_2}} = \frac{F \times [(E_{E1} + E_{E2}) \times I_{\text{cell}}]}{I_{\text{cell}} \times M_{\text{CO}_2} \times \eta_{\text{current}} \times \eta_{\text{precipitate transfer}}} \quad (\text{E28})$$

Techno-economic analysis (TEA):

The techno-economic analysis of the DAC plant equipped with the cyclic viologen electrocatalysis configuration was performed. The assumptions were provided as follows:

- A DAC plant capacity of 100 tCO₂, operating 365 days per year, and a current efficiency of 90%.
- The operation lifetime of all CAPEX equipment is 20 years.
- The project discount rate is set at 10%.
- A cost-to-capacity method (CtCM) was employed in this TEA.¹² To estimate the air contactor cost, a scaling factor of 0.9 was applied for scaling down from a 1Mt scale to a 100t scale. A scaling factor of 0.8 was utilized to estimate the costs of catalysts, membranes, and chemicals from laboratory scale up to a 100t scale.
- The price of LiCl is estimated to be \$500 per kilogram and the price of viologen is estimated to be \$91.6 per gram.
- The present lifespan of the proton exchange membrane water electrolysis is 4 years, and the current density stands at 1000 mA cm⁻².¹³ Therefore, the catalyst and membrane degradation rate are estimated as 2.5 x 10⁻⁴ mA⁻¹ yr⁻¹.
- The renewable electricity is from onshore wind project with a price of \$35/MWh.¹⁴
- With additional system optimization. The annual chemical replacement constitutes 20% of the total chemical.

Project scope:

CAPEX cost includes	Air Contactor, CVE system, neutralization solution tank, chemical cost, and balance of plant (BOP)
OPEX cost includes	Electrical energy, process water, chemical replacement, catalyst and membrane replacement, and others

Summary of carbon removal project cost:

CAPEX cost type:	Total cost (\$ initial)	Cost per tCO₂
Air contactor	33,358	16.7
CVE system (at 40 mA cm ⁻²)	29,160	14.6
Neutralization solution tank	2,000	1.0
Chemical cost	82,045	41.0
Balance of plant (BOP)	14,656	7.3
Net	161,219	80.6

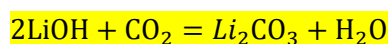
OPEX cost type:	Total cost (\$ initial)	Cost per tCO₂
Electricity (at 5 GJ per tCO ₂)	5,348	53.5
Process water	100	1.0
Chemical replacement	16,409	164.1
Catalyst replacement	6,852	68.5
Others	2,871	28.7
Net	31,579	315.8

NPV of net cost per ton CO₂ (@ 10% discount rate): \$238

Detailed TEA calculations:

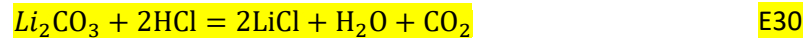
2 moles of OH⁻ are needed to capture 1 mole of CO₂ (E29). The CO₂ capture rate is specified as 12.68 kgCO₂ h⁻¹ to achieve an annual capture of 100 tCO₂ per year (E32). Converting this rate yields 288.18 molCO₂ h⁻¹ and 576.36 molOH h⁻¹, as indicated in equations (E33), (E34).

Air contactor:



E29

Neutralization solution tank:



CVE system:



$\frac{100tCO_2}{1yr} \times \frac{1yr}{8760h} \times \frac{1000kg}{1t} \div 0.9 = 12.68 \left[\frac{kgCO_2}{h} \right]$	E32
$\frac{12.68 kgCO_2}{1 h} \times \frac{1000 g}{1 kg} \times \frac{1 mol}{44 g} = 288.18 \left[\frac{molCO_2}{h} \right]$	E33
$\frac{288.18 molCO_2}{h} \times 2 = 576.36 \left[\frac{molOH}{h} \right]$	E34

Faraday's law is applied to calculate the CVE total current needed, where the total current needed is

30875.2A, as indicating from equation (E35):

$$I = 576.36 \left[\frac{molOH}{h} \right] \times \frac{1[h]}{3600[s]} \times nF \times 2 = 30875.2[A] \quad E35$$

The power needed is calculated by using equation (E36).

$$P = 1.05 [V] * 30875.2[A] = 32.4 [kW] \quad E36$$

CAPEX calculation:

Air contactor CAPEX: The capital cost for an air contactor at 1Mt scale is ~ \$132.8 million, including all engineering, procurement, construction fees.¹⁵ Utilizing the CtCM, the estimated CAPEX for a 100t scale air contactor is projected to be **\$33,358**.

CVE system CAPEX: The scope of the CVE System encompasses various components, including frame, plates, assembly & endplates, balance of stack, power supplied, deionized water circulation, and miscellaneous, as outlined in the NREL study.¹⁶ The estimated cost for the electrolyzer is \$600/kW. Considering our system's configuration as a tri-electrode system, the estimated CVE cost is \$900/kW. Considering a power requirement of 32.4 kW for a 100t scale CVE system. The estimated CAPEX for CVE system is projected to be **\$29,160**.

Neutralization solution tank CAPEX: The neutralization solution tank comprises an electrical mixer and a water tank. The estimated CAPEX for neutralization solution tank is projected to be **\$2,000**.

Chemical CAPEX: All chemicals undergo recycling, and with an initial volume of 50 liters in the neutralization solution tank. The required amounts for 2M LiCl chemical and 0.2M viologen chemical are 4.25kg and 4.9 kg, respectively. The viologen cost from lab-scale to large scale was determined using the CtCM. The estimated CAPEX for a 100t scale chemical is projected to be **\$82,045**.

BOP CAPEX: The BOP is assumed to be 10% of the total CAPEX, the estimated CAPEX for a 100t scale BOP is projected to be **\$14,656**.

OPEX calculation:

Electrical energy OPEX: The energy cost for the CVE system is 5 GJ per tCO₂. An additional 10% of electrical energy is consumed, covering liquid pumps and electrical controls. The total electrical energy usage is 152.8 MWh. The estimated OPEX for a 100t scale electrical energy is projected to be **\$5,348**.

Process water usage OPEX: Process water is required for air contactor evaporative losses, the water consumption is 4.74 tH₂O/tCO₂.¹⁵ The cooling water price is \$0.21/m³. The estimated OPEX for a 100t scale process water usage is projected to be **\$100**.

Chemical OPEX: The annual chemical replacement is expected to be 20%. The estimated OPEX for a 100t scale chemical is projected to be **\$16,409**.

Catalyst and membrane OPEX: The catalyst and membrane cost from lab scale to pilot scale was determined using CtCM. We assumed that catalyst and membrane materials will be more costly than average materials and therefore will use 0.8 as the scale factor.

Material	Ni/Fe Foam	Carbon electrode	Platinum on Vulcan	N115 w/ PtB	N115
Lab-scale cost	488 [\$ m ⁻²]	770 [\$ m ⁻²]	9679 [\$ m ⁻²]	4107 [\$ m ⁻²]	1928 [\$ m ⁻²]

Given that our system operates at 40 mA cm^{-2} , with the degradation rate of $2.5 \times 10^{-4} \text{ mA}^{-1} \text{ yr}^{-1}$. The estimated OPEX for a 100t scale catalyst and membrane is projected to be **\$6,852**.

Others OPEX:

The others operational costs included transportation and maintenance. Assumption of 10% of total OPEX. The other OPEX is estimated to be **\$2,871**.

Table S1: Summary of electrochemical DAC/DOC capture and release methods

	CO ₂ source solution	Catholyte pH	Anolyte pH	Current density applied in energy calculation (mA cm ⁻²)	Experimental work inputs (GJ/t CO ₂)
Traditional alkaline sorbent regeneration ¹⁷	Carbonate	13	6.5	10	10.4
Fuel cell concentrator ¹⁸	Carbonate			0.5	7.9
DAC using Bipolar membrane electro dialysis (BPMED) ¹⁹	Carbonate	11.6	2.5	8.6	10.5
Alkaline sorbent regeneration through double CEM ²⁰	46% v/v Bicarbonate + 54% v/v Carbonate	13.1	6.8	2.5	8.5
Alkaline sorbent regeneration through anion exchange resin ²¹	46% v/v Bicarbonate + 54% v/v Carbonate	13	10	5	8.5
Iodide alternating electrocatalysis ²²	Carbonate	13	1.2	10 - 200	6.1 – 7.8
Porous solid-electrolyte reactor ²³	Carbonate	/	4	0.5 - 3	4.5 – 6.8
HCl intercalation pH-swing ²⁴	Bicarbonate	10	5	1	2.8

Ferricyanide coupled DOC using BPMED ²⁵	Bicarbonate	8.2	2.3	3.3	3.5
Neutral red organic PCET ²⁶	/	/	/	0.03	1.48
This work	Carbonate	13.3	2.8	10 - 120	3.8 – 8.5
This work	Bicarbonate	13.3	2.8	10 - 120	1.9 – 4.3

Table S2: Summary of organic electrochemical carbon capture and release methods

Organic Redox-active molecules	Mechanism	CO ₂ separation work inputs (GJ tCO ₂ ⁻¹)	Current density (mA cm ⁻²)	DAC applicability	Organic redox molecule exposed to capture stream
Anthraquinone (AQ) ²⁸	Quinone-based direct electro-swing	1.28	< 1	No	Yes
Poly-1,4-anthraquinone (PAQ) ²⁹	Quinone-based direct electro-swing	0.98 – 2.05	< 1	No	Yes
4,4'-bipyridine ³⁰	Bipyridine-based direct electro-swing	1.52	< 1	No	Yes
4,4'-azopyridine (AzPy) ³¹	Bipyridine-based direct electro-swing	2.72	2	No	Yes
Ethylenediamine ³²	EMAR	0.68 – 2.57	3 - 12	No	Yes
3,3'-(phenazine-2,3-diylbis(oxy)) bis(propane-1-sulfonate) (DSPZ) ¹¹	Phenazine-based indirect pH-swing	1.39 – 3.30	20 - 150	No	Yes
1 – amino pyridinium (1-AP) ³³	Pyridinyl-based indirect pH-swing	2.29 (CO ₂) 3.68 (DAC)	< 1	Yes	Yes
Neutral red (NR) ²⁶	Phenazine-based-indirect pH swing	0.80 (CO ₂) 1.48 (DAC)	< 1	Yes	Yes
This work	Bipyridine-based indirect pH-swing	0.82 (DAC)	< 1	Yes	No
This work	Bipyridine-based indirect pH-swing	3.8 – 8.5	10 – 120	Yes	No

Reference:

1. Kresse G, Furthmüller J. Efficiency of ab-initio total energy calculations for metals and semiconductors using a plane-wave basis set. *Comput Mater Sci.* 1996;6(1):15–50.
2. Kresse G, Hafner J. Ab initio molecular dynamics for liquid metals. *Phys Rev B.* 1993;47(1):558–61.
3. Payne MC, Teter MP, Allan DC, Arias TA, Joannopoulos JD. Iterative minimization techniques for ab initio total-energy calculations: Molecular dynamics and conjugate gradients. *Rev Mod Phys.* 1992;64(4):1045–97.
4. Kresse G, Furthmüller J. Efficient iterative schemes for ab initio total-energy calculations using a plane-wave basis set. *Phys Rev B Condens Matter Mater Phys.* 1996;54(16):11169–86.
5. Blöchl PE. Projector augmented-wave method. *Phys Rev B.* 1994;50(24):17953–79.
6. Joubert D. From ultrasoft pseudopotentials to the projector augmented-wave method. *Phys Rev B Condens Matter Mater Phys.* 1999;59(3):1758–75.
7. Pack JD, Monkhorst HJ. “special points for Brillouin-zone integrations”-a reply. *Phys Rev B.* 1977;16(4):1748–9.
8. Grimme S, Antony J, Ehrlich S, Krieg H. A consistent and accurate ab initio parametrization of density functional dispersion correction (DFT-D) for the 94 elements H-Pu. *Journal of Chemical Physics.* 2010;132(15).
9. McCrory CCL, Jung S, Peters JC, Jaramillo TF. Benchmarking heterogeneous electrocatalysts for the oxygen evolution reaction. *J Am Chem Soc.* 2013;135(45):16977–87.
10. Bertuzzi MA, Armada M, Gottifredi JC. Caracterización físico-química de soluciones de goma brea. XXII Interamerican Congress of Chemical Engineering, CIIQ 2006 and V Argentinian Congress of Chemical Engineering, CAIQ 2006 - Innovation and Management for Sustainable Development. 2006;49:1705–23.
11. Jin S, Wu M, Gordon RG, Aziz MJ, Kwabi DG. PH swing cycle for CO₂ capture electrochemically driven through proton-coupled electron transfer. *Energy Environ Sci.* 2020;13(10):3706–22.
12. Clayton T, Baumann PE. Cost-to-Capacity Method: Applications and Considerations. *The M&TS Journal* [Internet]. 2014;30(1):1–56. Available from: https://evcvaluation.com/wp-content/uploads/2019/06/Cost-to-Capacity-Method_Applications-and-Considerations.pdf
13. Schmidt O, Gambhir A, Staffell I, Hawkes A, Nelson J, Few S. Future cost and performance of water electrolysis: An expert elicitation study. *Int J Hydrogen Energy* [Internet]. 2017;42(52):30470–92. Available from: <https://doi.org/10.1016/j.ijhydene.2017.10.045>
14. IRENA. Renewable Generation Costs in 2022. International Renewable Energy Agency.

2022. 69 p.
15. Keith DW, Holmes G, St. Angelo D, Heidel K. A Process for Capturing CO₂ from the Atmosphere. *Joule* [Internet]. 2018;2(8):1573–94. Available from: <https://doi.org/10.1016/j.joule.2018.05.006>
 16. Mayyas A, Ruth M, Pivovar B, Bender G, Wipke K, Mayyas A, et al. Manufacturing Cost Analysis for Proton Exchange Membrane Water Electrolyzers. National Renewable Energy Laboratory [Internet]. 2019;(August):65. Available from: <https://www.nrel.gov/docs/fy10osti/72740.pdf>.%0Ahttps://www.nrel.gov/docs/fy10osti/72740.pdf.%0Ahttps://www.nrel.gov/docs/fy10osti/72740.pdf.%0Ahttps://www.nrel.gov/docs/fy10osti/72740.pdf
 17. Stucki S, Schuler A, Constantinescu M. Coupled CO₂ recovery from the atmosphere and water electrolysis: Feasibility of a new process for hydrogen storage. *Int J Hydrogen Energy*. 1995;20(8):653–63.
 18. Laudon Matthew, Laird DL, Romanowicz BF, NSTI Nanotechnology Conference and Trade Show (2009 : Houston Tex), TechConnect Summit (2009 : Houston Tex). *Clean Technology 2009 : bioenergy, renewables, storage, grid, waste and sustainability : technical proceedings of the 2009 CTSI Clean Technology and Sustainable Industries Conference and Expo, Clean Technology 2009 ... May 3-7, 2009, Houston, Texas, U.S.A.* 2009;396.
 19. Eisaman MD, Parajuly K, Tuganov A, Eldershaw C, Chang N, Littau KA. CO₂ extraction from seawater using bipolar membrane electrodialysis. *Energy Environ Sci*. 2012;5(6):7346–52.
 20. Shu Q, Legrand L, Kuntke P, Tedesco M, Hamelers HVM. Electrochemical Regeneration of Spent Alkaline Absorbent from Direct Air Capture. *Environ Sci Technol*. 2020;54(14):8990–8.
 21. Shu Q, Haug M, Tedesco M, Kuntke P, Hamelers HVM. Direct Air Capture Using Electrochemically Regenerated Anion Exchange Resins. *Environ Sci Technol*. 2022;56(16):11559–66.
 22. Xu Y, Liu S, Edwards JP, Xiao YC, Zhao Y, Miao RK. Regeneration of Direct Air CO₂ Capture Liquid via Alternating Electrocatalysis. *Joule*. 2023;7(February):1–11.
 23. Zhu P, Wu ZY, Elgazzar A, Dong C, Wi TU, Chen FY, et al. Continuous carbon capture in an electrochemical solid-electrolyte reactor. *Nature*. 2023;618(7967):959–66.
 24. Kim S, Nitzsche MP, Rufer SB, Lake JR, Varanasi KK, Hatton TA. Asymmetric chloride-mediated electrochemical process for CO₂ removal from oceanwater. *Energy Environ Sci*. 2023;2030–44.
 25. Digdaya IA, Sullivan I, Lin M, Han L, Cheng WH, Atwater HA, et al. A direct coupled electrochemical system for capture and conversion of CO₂ from oceanwater. *Nat Commun* [Internet]. 2020;11(1):1–10. Available from:

<http://dx.doi.org/10.1038/s41467-020-18232-y>

26. Seo H, Hatton TA. Electrochemical direct air capture of CO₂ using neutral red as reversible redox-active material. *Nat Commun.* 2023;14(1):1–11.
27. Gurkan B, Simeon F, Hatton TA. Quinone Reduction in Ionic Liquids for Electrochemical CO₂ Separation. *ACS Sustain Chem Eng.* 2015;3(7):1394–405.
28. Liu Y, Ye HZ, Diederichsen KM, Van Voorhis T, Hatton TA. Electrochemically mediated carbon dioxide separation with quinone chemistry in salt-concentrated aqueous media. *Nat Commun.* 2020 Dec 1;11(1).
29. Voskian S, Hatton TA. Faradaic electro-swing reactive adsorption for CO₂ capture. *Energy Environ Sci.* 2019;12(12):3530–47.
30. Ranjan R, Olson J, Singh P, Lorange ED, Buttry DA, Gould IR. Reversible Electrochemical Trapping of Carbon Dioxide Using 4,4'-Bipyridine That Does Not Require Thermal Activation. *Journal of Physical Chemistry Letters.* 2015;6(24):4943–6.
31. Li X, Zhao X, Liu Y, Hatton TA, Liu Y. Redox-tunable Lewis bases for electrochemical carbon dioxide capture. *Nat Energy.* 2022;7(11):1065–75.
32. Rahimi M, Diederichsen KM, Ozbek N, Wang M, Choi W, Hatton TA. An Electrochemically Mediated Amine Regeneration Process with a Mixed Absorbent for Postcombustion CO₂ Capture. *Environ Sci Technol.* 2020;54(14):8999–9007.
33. Seo H, Rahimi M, Hatton TA. Electrochemical Carbon Dioxide Capture and Release with a Redox-Active Amine. *J Am Chem Soc.* 2022;144(5):2164–70.